

Mechanical Properties of Highly Deformable Elastomeric Gyroids for Multifunctional Capacitors

Emilie R. Baker, Khoi Ly, Nikola Bosnjak, Maura R. O'Neill, Rachel Miller, Sandra Li, Robert F. Shepherd,* and Meredith N. Silberstein*

Triply periodic minimal surface lattices have mechanical properties that derive from the unit cell geometry and the base material. Through computation software like nTopology and Abaqus, these geometries are used to tune non-linear stress–strain curves not readily achievable with solid materials alone and to change the compliance by two orders of magnitude compared to the constituent material. In this study, four elastomeric TPMS gyroids undergo large deformation compression and tension testing to investigate the impact of the structure's geometry on the mechanical properties. Among all the samples, the modulus at strain $\varepsilon = 0.05$ varies by over one order of magnitude (7.7–293.4 kPa from FEA under compression). These lattices are promising candidates for designing multifunctional systems that can perform multiple tasks simultaneously by leveraging the geometry's large surface area to volume ratio. For example, the architectural functionality of the lattice to bear loads and store mechanical energy along with the larger surface area for energy storage is combined. A compliant double-gyroid capacitor that can simultaneously achieve three functions is demonstrated: load bearing, energy storage, and sensing.

1. Introduction

A metamaterial derives its mechanical properties not only from its material but also from its geometry.^[1–3] Applications include tissue engineering,^[4–6] actuators,^[7–13] heat exchangers,^[14,15] and energy storage devices.^[16,17] Metamaterials can modify the mechanical,^[18–24] electrical,^[16,17,25] acoustic,^[26–31] optical,^[32–34] fluidic,^[35,36] and thermal^[14,15,37] behavior of devices and structures. Triply periodic minimal surface (TPMS) lattices are a well defined subcategory of metamaterials. TPMS refers to geometry that repeats in three dimensions (triply periodic), and the surface

has a constant mean curvature of zero at every point (minimal surface).^[38]

The goal of this work is to show how TPMS lattices stand out from other metamaterials as promising candidates for multifunctional system designs using both their mechanical robustness (for mechanical tuning of a structure) and importantly their large surface area to volume ratio. TPMS lattices can make 1) mechanically robust composites because of how they separate space into continuous and intertwined regions and 2) valuable multiphysics systems because of their large surface area to volume ratio. Large surface area creates a larger interaction site that can be leveraged in different energy domains for increased chemical activity, faster diffusion rates, faster heat transfer, larger electric fields, and larger magnetic fields. Multifunctional systems and embodied energy systems, systems that combine structural functionality with energy


storage,^[39] are attractive solutions for addressing the limited onboard energy storage, adaptability, functionality, and efficiency of devices and robots.

In this article, we look at the TPMS lattice known as the gyroid, which was discovered by Alan Schoen in 1970.^[40] The equations shown in **Figure 1Ai** approximate the gyroid's geometry. First, we study the mechanical properties of the gyroid. We wrote Python scripts to automate commercial software for easy to produce 3D printer files and finite-element (FE) mesh files. After generating the FE mesh files, a second software script runs a finite-element analysis (FEA) for both compression and tension loading conditions with strains of $\varepsilon = \pm 0.5$. We define strain as $\varepsilon = \Delta H \times H_0^{-1}$ where H is height. We analyze four different gyroid unit cells. The lattices are composites of elastomer and air.

TPMS structures often have complex geometries that are more easily fabricated with additive manufacturing. Advances in digital light processing (DLP), a type of 3D printing, enable a range of materials to be 3D printed, including resilient elastomers. By producing elastomeric lattice structures, we are able to tune mechanical properties by leveraging: 1) the elastomeric material's ability to return to the undeformed configuration after removing loads and 2) the TPMS structure's ability to tune the stress–strain response. As DLP printers are limited in their ability to produce resilient multimaterial parts, the utility of the lattices affects similar outcomes as multimaterials while

E. R. Baker, K. Ly, N. Bosnjak, M. R. O'Neill, S. Li, R. F. Shepherd, M. N. Silberstein
Department of Mechanical and Aerospace Engineering
Cornell University
Ithaca, NY 14850, USA
E-mail: rfs247@cornell.edu; ms2682@cornell.edu

R. Miller
Department of Materials Science and Engineering
Cornell University
Ithaca, NY 14850, USA

 The ORCID identification number(s) for the author(s) of this article can be found under <https://doi.org/10.1002/adem.202300629>.

DOI: 10.1002/adem.202300629

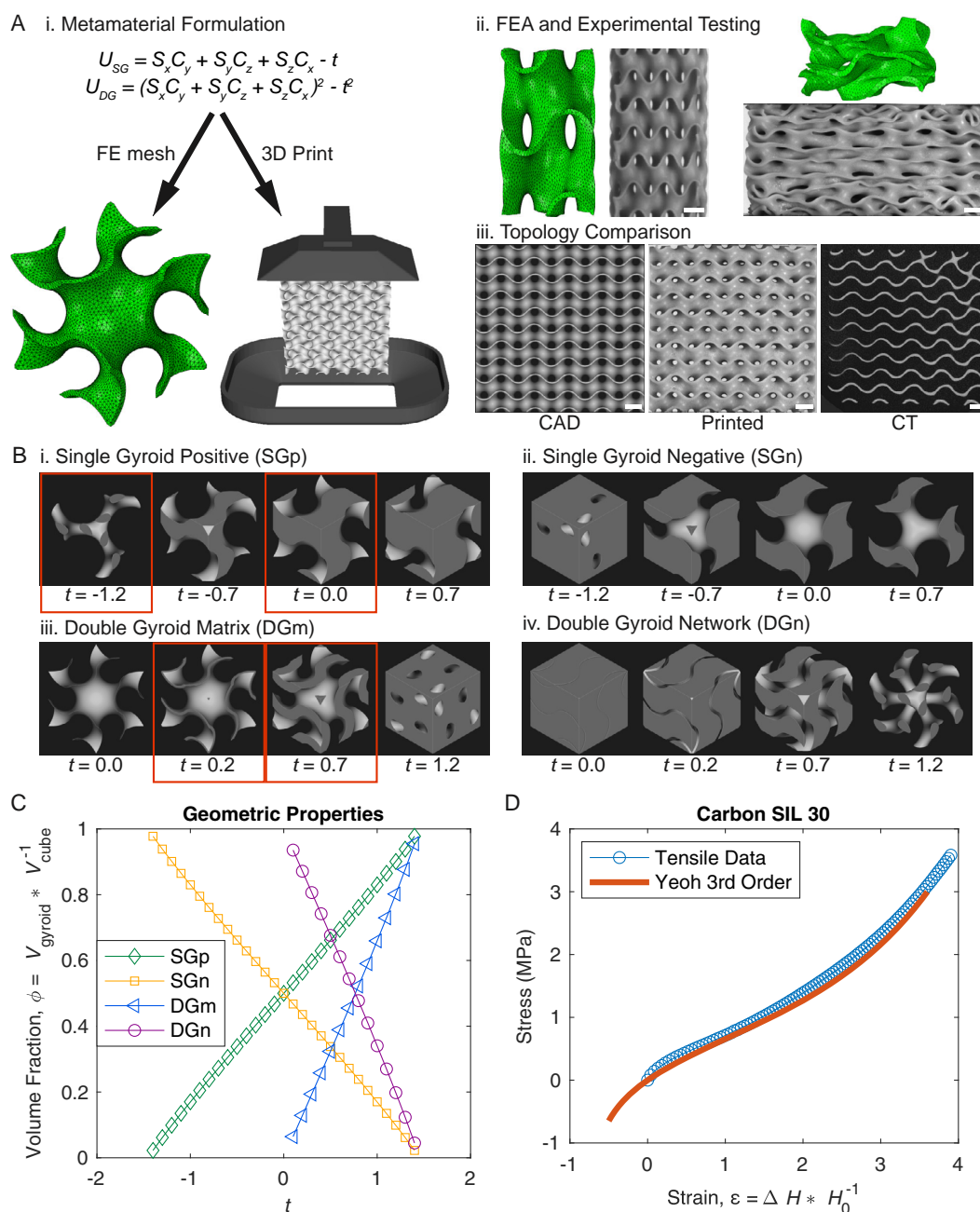


Figure 1. A) Project overview: (Ai) Software shows the equations for the gyroid in nTopology to generate the FE mesh (green image) and the files for 3D printing. (Aii) The software takes the FE mesh files and runs a tension and compression analysis (green images). 3D-printed samples undergo equivalent experimental test conditions to validate the FEA models. (Aiii) CT scans of the 3D-printed specimen compared to the computer-generated models. B) Computer-generated gyroids include: (Bi) single-gyroid-positive SGp, (Bii) single-gyroid-negative SGn, (Biii) double-gyroid matrix DGm, and (Biv) double-gyroid-network DGn. For each geometry, the corresponding t values from the equations in Ai are given. These images demonstrate how the gyroid changes with t . The four gyroids studied are outlined in red boxes. C) Trends between the volume fraction and the gyroid equation parameter t . D) Mechanical properties of SIL 30 and the Yeoh third-order material model. Tensile data provided by Carbon 3D Inc.

using only one chemistry in addition to producing nonlinear stress–strain curves not readily achievable with either solid materials or multimaterial parts. Experimental tests using 3D-printed silicone urethane elastomeric parts validate the FEA results. Figure 1A provides the project overview.

The most compliant and most stiff gyroids have a modulus at $\varepsilon = 0.05$ that varies by over one order of magnitude (7.7–293.4 kPa under compression and 10.7–282.1 kPa under tension) for volume fractions, $\phi = V_{\text{gyroid}} / V_{\text{cube}}$, between 0.1 and 0.46 (where V_{gyroid} is volume occupied by the gyroid and

V_{cube} is the volume of the cube enclosing the gyroid). Using the mechanical analysis, we design, print, and test a compliant gyroid capacitor. The capacitor is a multifunctional embodied energy system because it combines structural functionality (large compliance), electrical energy storage (capacitor), and self-sensing (ability to measure changes in capacitance with deformation).

2. Experimental Section

2.1. Designing Gyroids

TPMS geometries, like the gyroid, can be approximated using mathematical equations.^[41,42] Equation (1) defines the surface of the single gyroid in 3D space

$$U_{\text{SG}}(x, y, z) \equiv S_x C_y + S_y C_z + S_z C_x = t \quad (1)$$

where t is a function of the volume fraction. S and C are short hand notations for sine and cosine.

$$S_i = \sin(k_i i L_i^{-1}) \text{ (with } i = x, y, z) \quad (2)$$

$$C_i = \cos(k_i i L_i^{-1}) \text{ (with } i = x, y, z) \quad (3)$$

where x , y , and z are coordinate directions, and L_i is the length of the unit cell in each direction. k_i is the lattice function periodicity

$$k_i = 2\pi n_i \text{ (with } i = x, y, z) \quad (4)$$

where n_i is the number of unit cells in each direction. Equation (1) produces the geometries in Figure 1Bi,ii and divides space into two regions. We indicated the region formed by Figure 1Bi as single-gyroid positive (SGp) and the void region as single-gyroid negative (SGn) in Figure 1Bii. SGp and SGn had opposite chirality, and if added together, they formed a solid cube given the same t value. The double gyroid (DG) divides space into three regions. The matrix (DGm) separates two void regions that form two separate networks (DGn), as shown in Figure 1Biii–iv. The following Equation (5) defines the surface of the double gyroid

$$U_{\text{DG}}(x, y, z) \equiv (S_x C_y + S_y C_z + S_z C_x)^2 = t^2 \quad (5)$$

where t is once again directly related to the volume fraction. Equation (5) produces the geometries in Figure 1Biii–iv. Figure 1C shows the correlation between t and volume fraction.

nTopology, a commercial software, can define geometry by mathematical expressions. Scripting nTopology automates the production of many geometry variations quickly and easily by controlling inputs like the equation. We selected four gyroid variations for this study including SGp (with t values equal to -1.2 and 0.0) and DGm (with t values equal to 0.2 and 0.7). **Table 1** lists the naming convention and volume fraction of elastomer. We studied SGp and DGm because they were the base components of all the gyroid variations. For example, SGn had opposite chirality from SGp, and DGn was the combination of SGp and SGn (given the corresponding t parameters like SGp-1.2 and SGn1.2). Additionally, we selected SGp and DGm lattices to provide cleaner and more reliable results for both printing and

Table 1. Gyroid variations.

Name	Gyroid	t	Volume Fraction [ϕ]
SGp-1.2	SGp	-1.2	0.1
SGp0.0	SGp	0.0	0.5
DGm0.2	DGm	0.2	0.13
DGm0.7	DGm	0.7	0.46

simulation of low- and high-volume-fraction lattices. For printing the DGn, more fabrication challenges arise for low volume fractions (smaller struts) and high volume fractions (preventing connections between networks). For simulations, two networks lead to more contact interactions, which can greatly increase the computational cost and make convergence more difficult. In this study, the length of the unit cells, L_i , was 10 mm in each direction (x, y, z). We chose the values of t and L_i based upon printability and interest in looking at highly compliant, porous structures. After defining the geometric parameters, the software exported print files (.stl) and finite-element mesh files (.inp for Abaqus).

2.2. FEA Simulations

By scripting Abaqus, a commercial FEA software, the user could automate FEA with Python programming language. The material model used to approximate the behavior of the elastomer was a Yeoh third-order hyperelastic material model. Figure 1D shows a good fit between the material model and the experimental tension data supplied by Carbon 3D for SIL-30, a silicone urethane elastomer. The mesh file from nTopology consisted of linear tetrahedral hybrid elements (C3D4H). To reduce computation time, the analysis used a single-unit cell of each gyroid. We applied periodic boundary conditions (PBCs) to account for the larger system of the composite. To apply PBCs, dummy nodes constrained the nodes on the corners, edges, and faces of the unit cells.^[43,44] The dummy nodes were either free, fixed, or stepped to 5 mm of displacement ($\epsilon = 0.5$ engineering strain) to mimic the compression and tension boundary conditions of the experimental tests (Figure S1, Supporting Information). Finally, contact interactions prohibited self penetration as the geometry deforms.

2.3. Experimental Testing

The experimental compression samples consisted of $5 \times 5 \times 5$ unit cells, which resulted in dimensions of $50 \times 50 \times 50$ mm. The experimental tension samples consisted of $3 \times 3 \times 10$ unit cells, which resulted in dimensions of $30 \times 30 \times 100$ mm. For each test mode, compression and tension, there were three specimens for each geometry listed in Table 1. We printed, cured, and tested every sample in the z -direction as defined by Equation (1) and (5). We used a Carbon 3D M1 printer with SIL 30 (a silicone urethane resin) for printing, cleaned the parts with isopropyl alcohol for 5 min, left the parts dry for at least 12 h, and then placed the parts in a salt bath during heat treatment (8 h at 120°). The salt bath was for preserving the dimensions and shape of the samples during heat treatment. For the experimental

setup, we used a Zwick/Roell Z10 testing system, with a 500 N load cell, that collected force and strain data. The specimens underwent three cycles at a strain rate of $1\% \text{ s}^{-1}$ until $\epsilon = 0.5$ was reached. To understand some of the discrepancies between the FEA and the experimental results, micro-computed tomography (μCT) scans provided visual understanding to identify the differences between the 3D-printed and computer-generated structures.

2.4. Capacitors

Capacitance, for example, can be increased by having larger surface area electrodes. Using equations not specific to any geometry, the equation for capacitance is

$$C = Q|\Delta V|^{-1} \quad (6)$$

where Q is the charge, and ΔV is the potential difference. Potential difference is given by

$$\Delta V = V_- - V_+ = \int_+^- \mathbf{E} d\mathbf{l} \quad (7)$$

where \mathbf{E} is electric field, and $d\mathbf{l}$ is the differential displacement vector between the positive and negative electrodes. We can calculate the electric field everywhere using Gauss's law.

$$\oint \mathbf{E} d\mathbf{A} = Q\epsilon_r^{-1}\epsilon_0^{-1} \quad (8)$$

where $d\mathbf{A}$ is an infinitesimal amount of area on the surface, Q is charge, ϵ_r is relative permittivity, and ϵ_0 is vacuum permittivity. From these equations, the larger the surface area of the electrodes and/or smaller the distance between the electrodes, the larger the capacitance. To demonstrate both the mechanical robustness and large surface area, we fabricated a gyroid capacitor.

A compliant capacitor demonstrates the multifunctionality of the gyroid lattice and consists of three sections. One section is the capacitor: a double-gyroid network with a t value equal to 1.2 (DGN1.2). The DGN1.2 consisted of $1 \times 3 \times 3$ unit cells resulting in dimensions of $10 \times 30 \times 30$ mm. The other two sections were solid rectangular prisms for applying loads in the FEA or for gripping the physical device in tension during the experiment. For the FEA of the device, we created the mesh file for the DGN1.2 with $1 \times 3 \times 3$ unit cells using nTopology. Next, Abaqus used the finite-element mesh for pulling the capacitor in tension. We fixed one solid rectangular prism and applied a displacement in 1 mm increments to the other prism. Then, we used COMSOL multiphysics, a finite-element software. COMSOL calculates the capacitance with an electrostatics analysis using the deformed mesh files (relative permittivity of 3.2 for the dielectric and 1 for the electrodes). To validate the FEA results, we performed an experiment. We printed the DGN1.2 capacitor with the same material and processed as the rest of the parts in this article, and afterward, we applied carbon paint (DAG-T-502, TED PELLA INC.) onto the networks using a brush. The carbon paint made the network conductive and thus formed the compliant electrodes of the capacitor. For testing purposes, we used super glue to bond the device to a container that we filled with a vegetable-based liquid dielectric (Envirotemp FR3, $\epsilon_r = 3.2$). A handheld inductance (L),

capacitance (C), and resistance (R) (LCR) meter (KEYSIGHT U1733C) measured the capacitance at 10 kHz.

3. Results

3.1. Compression Results

In this section, we discuss the computational and experimental results of the four gyroid geometries in Table 1 under compression. Figure 2A,B and D–E contain computer-generated geometry (top left), the Von Mises stress from the FEA under $\epsilon = 0.5$ compression (top right), the 3D-printed $5 \times 5 \times 5$ unit cell specimen prior to being tested (bottom left), and the 3D-printed $5 \times 5 \times 5$ unit cell specimen under $\epsilon = 0.5$ compression (bottom right). The one exception is that the FEA data for SGp0.0 did not fully converge at $\epsilon = 0.5$ and so the last converged data at $\epsilon = 0.436$ was used for the FEA image in Figure 2D. Based on FEA models for each gyroid, the stress does not localize, with the exception of SGp0.0, which has localized large stress points where self contact occurs and likely causes convergence issues. Based on visual comparisons of the images, the FEA models capture the deformation obtained experimentally. DGM0.7 is a notable exception where the sinusoidal curves on the front face of the FEA model uniformly deform into each other. The uniformity and spacing do not match in the 3D-printed sample. The difference is from imperfections introduced during printing that causes misalignment of the sinusoidal curves, as seen in the specimen prior to being tested. While loading the sample in compression, DGM0.7 undergoes some shearing during the compression load as a result of the offset sinusoidal curves.

One interesting deformation feature worth noting is the deformation of DGM0.2. The structure tends toward a layer-by-layer collapse. The experimental samples display a tendency for unit cell layers near the compression plates to collapse prior to the middle layers. Similar deformation patterns for this structure are reported in literature for gyroids made from PA 2200 (nylon 12 thermoplastic)^[20,21] and metal.^[18] We believe the layers near the compression plates collapse first because they have the most distinct boundary conditions. Of course, this phenomenon does not occur in the FEA because there is only a single unit cell.

The plots in Figure 2C,F show the stress–strain curves for the data obtained from the FEA and experimental compression tests. We calculate stress as follows.

$$\sigma = F \times A_{\text{composite}}^{-1} \quad (9)$$

where F is force and $A_{\text{composite}}$ is the cross sectional area of the composite. For example, the cross-sectional area of one unit cell is 100 mm^2 ($10 \text{ mm} \times 10 \text{ mm}$), and the cross-sectional area of the $5 \times 5 \times 5$ samples is 2500 mm^2 ($50 \text{ mm} \times 50 \text{ mm}$). The 3D-printed specimens are compressed up to $\epsilon = 0.5$ and unloaded. The data is an average of three samples, and the error bars represent one standard deviation. The stress–strain curves have residual strain and hysteresis for every geometry, which results from the viscoelastic material as seen in Figure S2, Supporting Information. The one exception to this is the hysteresis of DGM0.2 where the geometry appears to have increased the amount of hysteresis. FEA models have corresponding

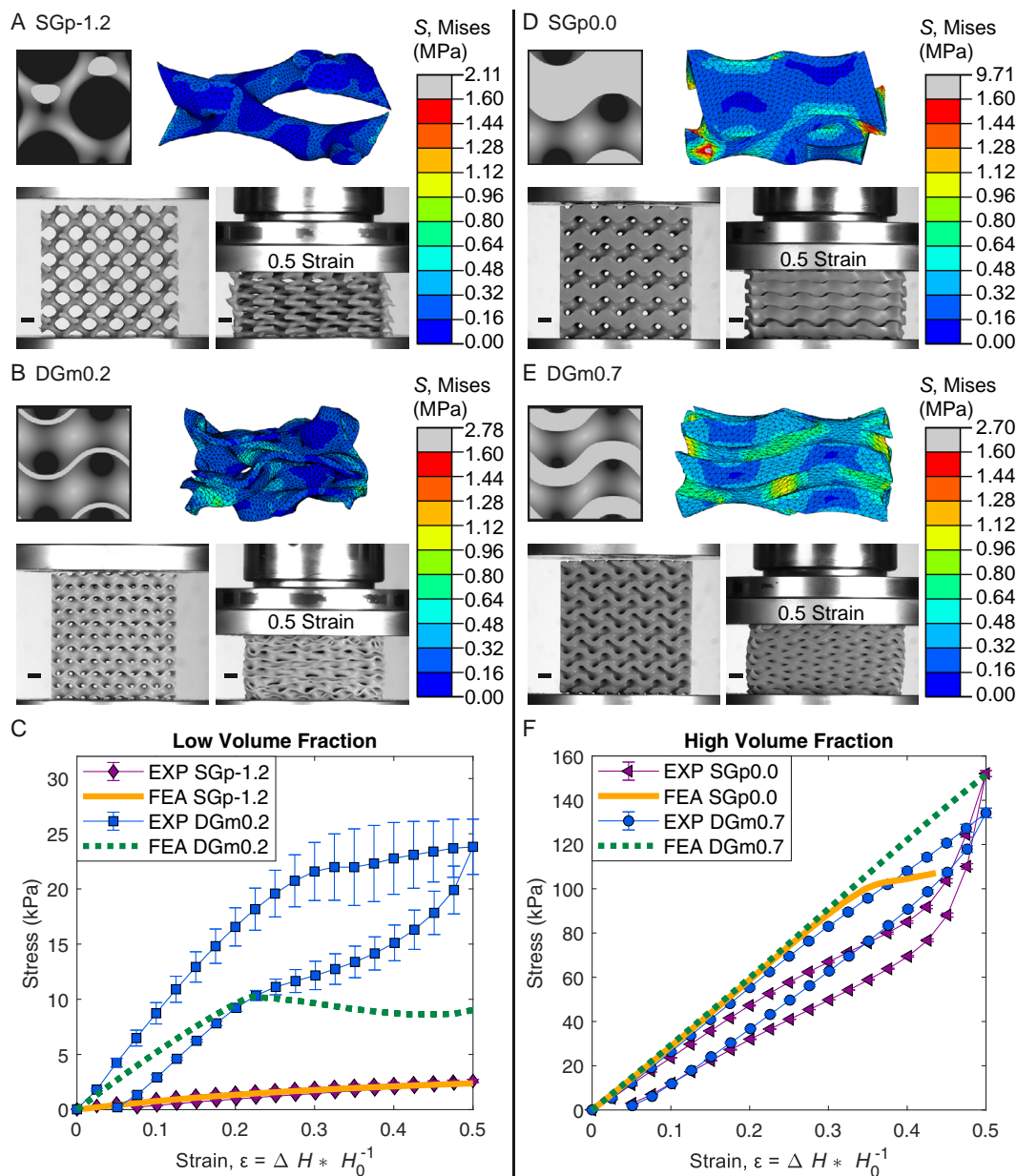


Figure 2. A–C) FEA and experimental data of the low-volume-fraction geometries under compression. The geometries include the SGp-1.2 ($\phi = 0.1$) and DGm0.2 ($\phi = 0.13$). (D–F) FEA and experimental data of the high-volume-fraction geometries under compression. The geometries include the SGp0.0 ($\phi = 0.5$) and DGm0.7 ($\phi = 0.46$). (A,B,D,E) Top left: Computer-generated geometry. Top right: Von Mises stress from the FEA under $\epsilon = 0.5$ (except SGp0.0 the last converged data/figure is at $\epsilon = 0.436$). Bottom left: 3D-printed $5 \times 5 \times 5$ unit cell sample before being tested. Bottom right: 3D-printed $5 \times 5 \times 5$ unit cell sample under $\epsilon = 0.5$. Scale bars are 5mm. C,F) Error bars represent one standard deviation, and the markers represent the average of three samples.

loading conditions up to $\epsilon = 0.5$. The unloading curves for the FEA models are not plotted as they follow the same path as the loading curves. Thus, the FEA models do not capture the hysteresis and residual strain of the material.

The low-volume-fraction structures in Figure 2C show that SGp-1.2 is the most compliant structure of all the gyroids with a computationally predicted modulus of 7.7 kPa at $\epsilon = 0.05$. Figure S3, Supporting Information, shows the curves for SGp-1.2 without DGm0.2 for better visualization. DGm0.2,

despite having only a slightly higher volume fraction ($\phi = 0.13$ compared to $\phi = 0.1$), is significantly stiffer than SGp-1.2 with a computationally predicted modulus of 51.9 kPa at $\epsilon = 0.05$. Studies^[45–47] report similar trends where the sheet geometry, which we refer to as the matrix in this article, has a higher stiffness than the network geometry (SGp, SGn, Dgn). Note that the stress–strain curve for DGm0.2 starts out with an approximately linear response and then becomes hypoelastic. The plateau in the curve corresponds to when the layers begin to

collapse onto each other. The high-volume-fraction geometries in Figure 2F are stiffer than the low-volume-fraction geometries. DGm0.7 is the stiffest gyroid with a computationally predicted modulus of 293.4 kPa at $\phi = 0.05$, and SGp0.0 is closely behind with a modulus of 286.5 kPa at $\phi = 0.05$. Therefore, SGp-1.2 is over an order of magnitude more compliant than DGm0.7. It is interesting to point out the experimental curve for SGp0.0 because the curve contains two distinctively different slopes ($\varepsilon = 0 - 0.35$ and $\varepsilon = 0.45 - 0.5$). The second slope of SGp0.0 approaches the slope of the solid SIL-30 from Figure 1D because after $\varepsilon = 0.45$ the gyroid has reached full collapse, and the structure behaves similarly to solid SIL-30. This also explains why the FEA solver struggles to converge after $\varepsilon = 0.436$ as a lot of contact occurs during full collapsing of the structure. Since the goal of the article is to study the mechanical properties of the gyroid and not the mechanical properties of the fully collapsed gyroid, the FEA data for $\varepsilon = 0 - 0.436$ is sufficient for our analysis.

3.2. Tension Results

In this section, we discuss the computational and experimental results of the four gyroids in Table 1 under tensile loads. Figure 3A,B and D–E show computer-generated geometry (top left), the von Mises stress from the FEA at $\varepsilon = 0.5$ (bottom left), the undeformed 3D-printed $3 \times 3 \times 10$ unit cell specimen (middle), and the 3D-printed $3 \times 3 \times 10$ unit cell specimen at $\varepsilon = 0.5$ (far right). Based on FEA models for each gyroid the stress does not localize and is fairly uniform throughout the structure, which indicates good stability for this geometry to support tensile loads. The FEA models capture the deformation obtained experimentally based on visual comparisons of the images.

The plots in Figure 3C,F show the stress–strain curves for the data obtained from the FEA and experimental tension tests. The 3D-printed specimens are pulled in tension up to $\varepsilon = 0.5$ and unloaded. The data is an average of three identical samples, and the error bars represent one standard deviation. The stress–strain curves have minor residual strain and hysteresis for every geometry, which results from the viscoelastic material, as shown in Figure S2, Supporting Information. FEA models have corresponding loading conditions up to $\varepsilon = 0.5$. The unloading curves for the FEA models are not plotted as they follow the same path as the loading curves. Thus, the FEA models do not capture the hysteresis and residual strain.

The low-volume-fraction geometries in Figure 3C show that SGp-1.2 is once again the most compliant of all the gyroids with a computationally predicted modulus of 10.7 kPa at $\varepsilon = 0.05$. Figure S3, Supporting Information, shows the curves for SGp-1.2 without DGm0.2 for better visualization. DGm0.2, despite having only a slightly higher volume fraction ($\phi = 0.13$ compared to $\phi = 0.1$), is significantly stiffer than SGp-1.2 with a computationally predicted modulus of 56.7 kPa at $\varepsilon = 0.5$. The high-volume-fraction structures in Figure 3F are stiffer than the low-volume-fraction structures. DGm0.7 is the stiffest gyroid with a computationally predicted modulus of 282.1 kPa at $\varepsilon = 0.05$, and SGp0.0 is closely behind with a modulus of 270.0 kPa at $\varepsilon = 0.05$. Table S1, Supporting Information, contains a complete list of modulus at $\varepsilon = 0.05$ for both the FEA and experimental data. The trend holds for

compression and tension data where the most compliant geometry, SGp-1.2, is more than an order of magnitude more compliant than the stiffest geometry, DGm0.7. The large difference in stiffness makes the gyroid a good choice for mechanically tuning parts and an alternative to multimaterial printing.

3.3. Discussion

Comparing the compression data to the tension data, Table S1, Supporting Information, shows that the computationally predicted modulus is higher in compression for the high-volume-fraction geometries of SGp0.0 and DGm0.7 whereas the computationally predicted modulus is higher in tension for the low-volume-fraction geometries of SGp-1.2 and DGm0.2. This data suggests that the higher-volume-fraction gyroids are stiffer in compression, and the lower-volume-fraction gyroids are stiffer in tension. The largest deviation between the computationally predicted modulus and the experimental modulus occurs with DGm0.2 geometry, which could be caused by a combination of misalignment of the porosity voids, worse printing resolution associated with the large surface area structure, parts being printed thicker than the CAD model, and the effects of the thickness increasing radially.

To understand the discrepancies between the FEA and experimental data, Figure S4, Supporting Information, shows a side-by-side comparison of the CAD models and the printed samples before testing. From these images notice that 1) SGp-1.2-printed part is thicker than the CAD model, 2) SGp0.0-printed part is thicker and the circular void regions are slightly misaligned, 3) the aligned, crisp void circles of DGm0.2 CAD model and the oval, misaligned voids of the printed DGm0.2, and 4) the large misalignment of the smaller voids for the DGm0.7 printed part. Additionally Figure S5, Supporting Information, provides CT scans for each of the gyroid compression samples. The visible discrepancy is that the thickness noticeably increases radially into the center of DGm0.2 and DGm0.7. The inconsistencies are from printer resolution and the inability to clean all the uncured resin off the parts before the thermal curing process. Another explanation for the discrepancies between the FEA data and the experimental data is due to the use of a representative volume element (RVE) (single-unit cell) and PBCs which are used to model an infinitely large structure. The experimental models, on the other hand, are composed of 125 unit cells which are not well representative of an infinite system. However, the benefit of choosing a single-unit cell and PBCs for simulations is to be able to run faster simulations so that this work can be extended to analyze a larger design space of geometries.

Gibson and Ashby provide a relationship between elastic modulus and volume fraction.^[48] The equation is

$$E_{\text{latt.}} = C_1 E_{\text{sol.}} \phi^n \quad (10)$$

where $E_{\text{latt.}}$ is the elastic modulus of the lattice, $E_{\text{sol.}}$ is the elastic modulus of the constituent material, C_1 is a prefactor, and n is a result of the deformation (stretch dominate ($n = 1$) or bending dominate ($n = 2$)). Fitting our single-gyroid data to the power law equation in Equation 10, we get $C_1 = 1.06$ and $n = 2.118$. Fitting our double-gyroid matrix data to the power law equation,

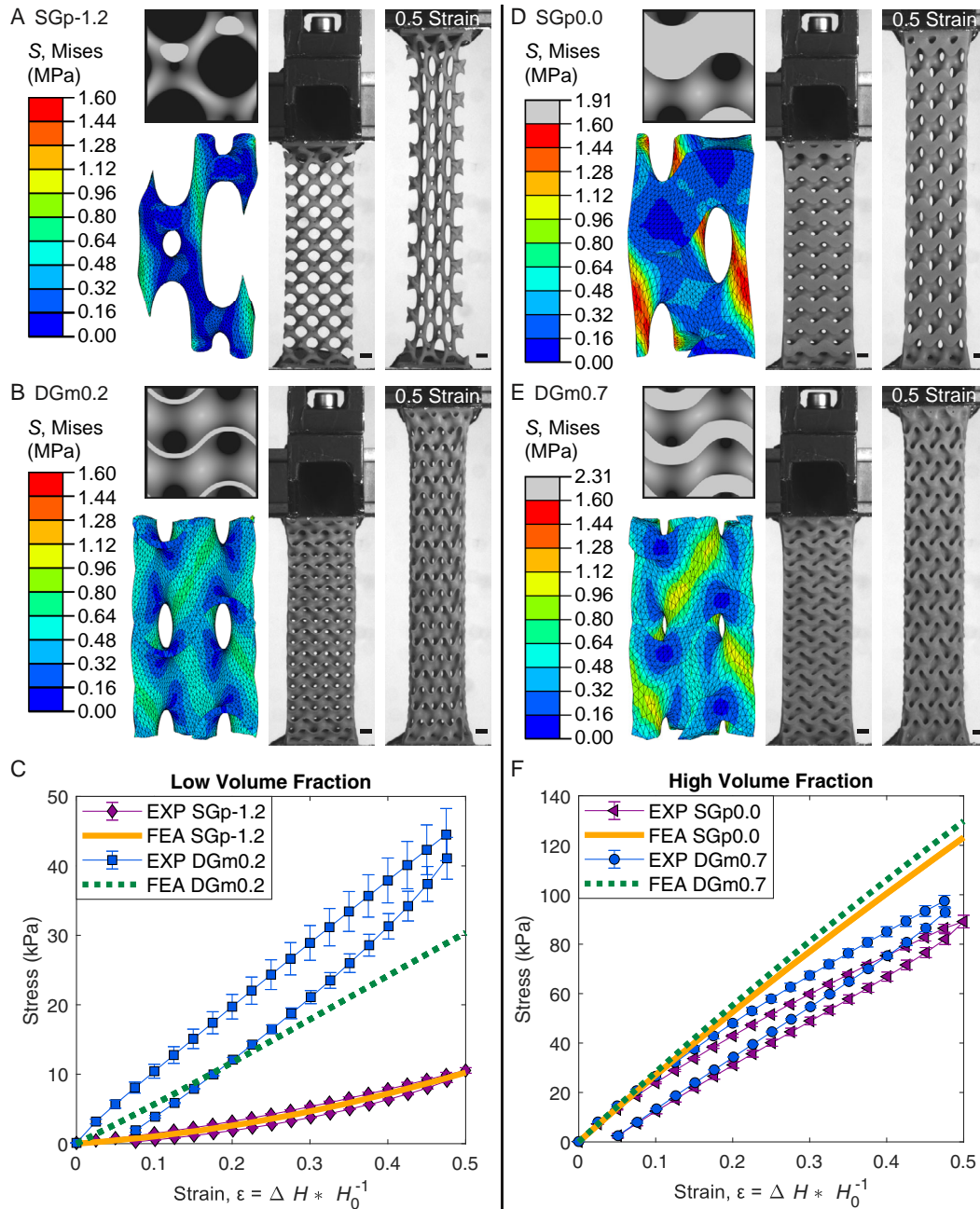


Figure 3. A–C) FEA and experimental data of the low-volume-fraction geometries under tension. The geometries include SGp-1.2 ($\phi = 0.1$) and DGm0.2 ($\phi = 0.13$). D–F) FEA and experimental data of the high-volume-fraction geometries under tension. The geometries include SGp0.0 ($\phi = 0.5$) and DGm0.7 ($\phi = 0.46$). A,B,D,E) Top left: Computer-generated geometry under no load. Bottom left: Von Mises stress from the FEA under $\varepsilon = 0.5$. Middle: 3D-printed $3 \times 3 \times 10$ unit cell sample before testing. Far right: 3D-printed $3 \times 3 \times 10$ unit cell sample under $\varepsilon = 0.5$. Scale bars are 5mm. C,F) Error bars represent one standard deviation, and the markers represent the average of three samples.

we get $C_1 = 0.703$ and $n = 1.32$. These values compare reasonably with other literature on gyroids, and the n values are reasonable for the dominant deformation mode expected for each gyroid type.^[19] reports a $C_1 = 1.02$ and $n = 2.4$ for single-gyroid geometry fabricated from PA2200, and^[20] reports a $C_1 E_{\text{sol}} = 892$ and $n = 1.39$ for double-gyroid matrix geometry made from PA2200.

3.4. Gyroid Capacitor

The compression and tension results show the gyroid's mechanical robustness as a composite. A second attractive quality of the gyroid is the large surface area to volume ratio. To demonstrate the novelty of using gyroid lattices for applications of multifunctional devices, we study a compliant gyroid capacitor.

A compliant capacitor has the ability to bear load, store energy, and sense deformation by measuring changes in capacitance.

First, we leverage the geometry and mechanical analysis study above to design a soft capacitor. SGp, SGn, and DGm cannot produce a capacitor on their own because a capacitor needs two electrodes. We could design a capacitor using any combination of SGp, SGn, and DGm together. Given that SGp-1.2 produces the most compliant structure, we chose to design the capacitor using SGp-1.2 and SGn1.2 which together form DGn1.2 (Figure 4A). While our previous mechanical experiments did not include DGn1.2, we hypothesize that the DGn1.2 force-strain curve would be approximately double that of the SGp-1.2 force-strain curve. We base the hypothesis on the fact that DGn1.2 contains the entire geometry of SGp-1.2 plus the SGn1.2 geometry. SGp-1.2 and SGn1.2 are similar in geometry, except that they have opposite chirality (given the corresponding t parameters). Experimental data in Figure S6, Supporting Information, supports our hypothesis that the force-strain curve for DGn1.2 is approximately double the force of the SGp-1.2 curve.

Figure 4B shows the experimental setup of the capacitor undergoing a tension test. Figure 4C shows the relative capacitance, $\Delta C \times C_0^{-1}$ where ΔC is change in capacitance and C_0 is capacitance under no tension. We measure the capacitance at different strains for two experiments and the FEA model.

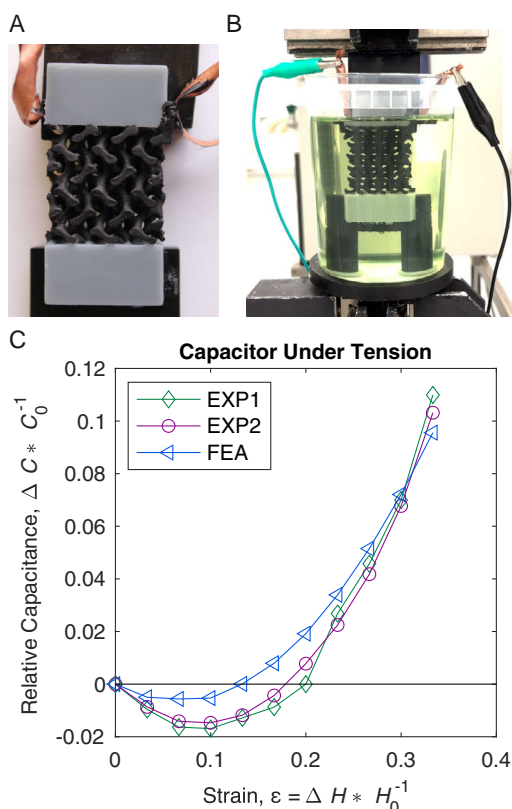


Figure 4. A) Double-gyroid capacitor with $t = 1.2$ ($\phi = 0.2$). We applied carbon paint to the networks. B) Experimental setup for measuring the capacitance as the capacitor is pulled in tension. C) Relative capacitance of DGn1.2 capacitor under different strains.

EXP1 and EXP2 are the experimental tests of the same sample retested. Overall, the experimental tests produce good repeatability with minimal discrepancies between the FEA data and the experiment. One interesting aspect of the overall trend is that the capacitance first decreases with strain and then increases with strain. For $\epsilon < 0.1$, the capacitance decreases with increasing strain. For $\epsilon > 0.1$, the capacitance increases with increases in strain. The factors contributing to this trend include the changes in surface area and the distance between the electrodes as the device is pulled in tension. Figure S7, Supporting Information, shows how surface area is changing with strain and capacitance as the capacitor undergoes tension. The effect of the distance between electrodes changing is much more challenging to measure as a result of the complex geometry and non-uniformity produced by the boundary conditions during tensile loading. Some of the discrepancies between the FEA and the experiment could be from the FEA assuming high conductivity and low resistivity of the electrode material, which is a good assumption for metals but can produce discrepancies for carbon paint. Additionally, in the experiment the electrode resistance varies as the double gyroid capacitor is stretched and there is likely an uneven coating of carbon paint. At $\epsilon = 0$, the FEA predicts 26.44 pF of capacitance, and the experiment predicts an average of 34.5 pF (as seen in Figure S8, Supporting Information). The mechanical response of the capacitor is in Figure S9, Supporting Information.

Here we demonstrate a capacitor over an order of magnitude more compliant than the constituent material and a surface area to volume ratio of 2.2 mm^{-1} (3893.2 mm^2 divided by 1750.3 mm^3). While we only study one combination of gyroid geometry for the multifunctional capacitor, other variations of SGp, SGn, DGm, and DGn could be studied. In summary, the DGn1.2 capacitor is a multifunctional embodied energy system whose structure is mechanically tuned for large compliance, geometry is a high surface area to volume ratio for producing a large capacitance, and structural deformation can be sensed from changes in capacitance.

4. Conclusion

TPMS geometries like the gyroid offer mechanically robust composite structures with high surface area-to-volume ratios for coupling multiple functionalities. We studied four different gyroid geometries where we show over that one order of magnitude difference in modulus is achievable between the most compliant and the stiffest gyroid studied. The FEA models show good visual deformation agreement with the deformed experimental samples. Given the lack of concentrated von Mises stress in the FEA models, the hyperelastic gyroids are robust structures under tension and compression loads. Using RVE and PBCs along with our scripted software, we have created a platform that can extend to other metamaterials and design optimization problems.

The double gyroid capacitor is a multifunctional device that embodies energy through the structural function of the gyroid (high compliance), storing electrical energy (large surface area to volume ratio of the gyroid structure), and sensing (estimating the deformation state by measuring the change in capacitance). The benefit of embodied energy systems is moving away from

traditional robots and devices with isolated power, actuation, sensing, and control and toward multifunctional systems that can perform multiple functions simultaneously. Applications for our capacitor include soft robotics and wearables because a capacitor is a fundamental building block for storing energy and a deformable capacitor is important for self-sensing of deformation.

Supporting Information

Supporting Information is available from the Wiley Online Library or from the author.

Acknowledgements

This work was supported in part by the National Science Foundation (NSF), contracts: 1825444 and IOS-2034351; NIH National Heart, Lung, and Blood Institute, contract: 5R01HL118019-07; Office of Naval Research, contract: N00014-22-1-2595; and Defense Advanced Research Project Agency Young Faculty Award, USA DARPA YFA, HR00112010004. This work made use of the Cornell Biotechnology Resource Center under the National Institutes of Health award No. S10OD025049. Air Force Office of Scientific Research, Contract: FA9550-19-1-0290.

Conflict of Interest

The authors declare no conflict of interest.

Data Availability Statement

The data that support the findings of this study are openly available in [Mechanical Properties of Highly Deformable Elastomeric Gyroids for Multifunctional Capacitors] at [10.5281/zenodo.7613347], reference number [7613347].

Keywords

additive manufacturing, elastomeric metamaterials, embodied energy, gyroid capacitors, triply periodic minimal surfaces

Received: May 3, 2023
Revised: June 28, 2023
Published online: July 18, 2023

- [1] K. Bertoldi, V. Vitelli, J. Christensen, M. v. Hecke, *Nat. Rev. Mater.* **2017**, 2, 17066.
- [2] M. Kadic, G. W. Milton, M. van Hecke, M. Wegener, *Nat. Rev. Phys.* **2019**, 1, 198.
- [3] S. C. L. Fischer, L. Hillen, C. Eberl, *Materials* **2020**, 13, 3605.
- [4] L.-Y. Zhu, L. Li, Z.-A. Li, J.-P. Shi, W.-L. Tang, J.-Q. Yang, Q. Jiang, *J. Transl. Med.* **2019**, 17, 89.
- [5] H. M. A. Kolken, S. Janbaz, S. M. A. Leeflang, K. Lietaert, H. H. Weinans, A. A. Zadpoor, *Mater. Horizons* **2018**, 5, 28.
- [6] J. M. Walker, E. Bodamer, A. Kleinfehn, Y. Luo, M. Becker, D. Dean, *Progr. Addit. Manuf.* **2017**, 2, 99.
- [7] J. I. Lipton, R. MacCurdy, Z. Manchester, L. Chin, D. Cellucci, D. Rus, *Science* **2018**, 360, 632.
- [8] D. Yang, B. Mosadegh, A. Ainla, B. Lee, F. Khashai, Z. Suo, K. Bertoldi, G. M. Whitesides, *Adv. Mater.* **2015**, 27, 6323.
- [9] M. Kaur, W. S. Kim, *Adv. Intell. Syst.* **2019**, 1, 1900019.
- [10] C. Tawk, R. Mutlu, G. Alici, *Front. Robot. AI* **2022**, 8, 799230.
- [11] T. Chen, M. Pauly, P. M. Reis, *Nature* **2021**, 589, 386.
- [12] H. Lee, Y. Jang, J. K. Choe, S. Lee, H. Song, J. P. Lee, N. Lone, J. Kim, *Sci. Robot.* **2020**, 5, aay9024.
- [13] Y.-L. Wei, Q.-S. Yang, L.-H. Ma, R. Tao, J.-J. Shang, *Mater. Des.* **2020**, 196, 109084.
- [14] J. Iyer, T. Moore, D. Nguyen, P. Roy, J. Stolaroff, *Appl. Therm. Eng.* **2022**, 209, 118192.
- [15] W. Li, G. Yu, Z. Yu, *Appl. Therm. Eng.* **2020**, 179, 115686.
- [16] J. G. Werner, G. G. Rodríguez-Calero, H. D. Abruña, U. Wiesner, *Energy Environ. Sci.* **2018**, 11, 1261.
- [17] D. Wei, M. R. J. Scherer, C. Bower, P. Andrew, T. Ryhänen, U. Steiner, *Nano Lett.* **2012**, 12, 1857.
- [18] I. Maskery, N. T. Aboulkhair, A. O. Aremu, C. J. Tuck, I. A. Ashcroft, *Addit. Manuf.* **2017**, 16, 24.
- [19] I. Maskery, L. Sturm, A. O. Aremu, A. Panesar, C. B. Williams, C. J. Tuck, R. D. Wildman, I. A. Ashcroft, R. J. M. Hague, *Polymer* **2018**, 152, 62.
- [20] D. W. Abueidda, M. Elhebeary, C.-S. A. Shiang, S. Pang, R. K. A. Al-rub, I. M. Jasiuk, *Mater. Des.* **2019**, 165, 107597.
- [21] D. W. Abueidda, M. Bakir, R. K. Abu Al-Rub, J. S. Bergström, N. A. Sobh, I. Jasiuk, *Mater. Des.* **2017**, 122, 255.
- [22] A. Ion, J. Frohnhofer, L. Wall, R. Kovacs, M. Alistar, J. Lindsay, P. Lopes, H.-T. Chen, P. Baudisch, in *Proc. of the 29th Annual Symp. on User Interface Software and Technology*, ACM, Tokyo Japan, **2016**, pp. 529–539.
- [23] C. El-Helou, R. L. Harne, *Adv. Eng. Mater.* **2019**, 21, 1900807.
- [24] S. Babaee, J. Shim, J. C. Weaver, E. R. Chen, N. Patel, K. Bertoldi, *Adv. Mater.* **2013**, 25, 5044.
- [25] M. R. O'Neill, D. Sessions, N. Arora, V. W. Chen, A. Juhl, G. H. Huff, S. Rudykh, R. F. Shepherd, P. R. Buskohl, *Adv. Mater. Technol.* **2022**, 2200296, 2200296.
- [26] S. Babaee, N. Viard, P. Wang, N. X. Fang, K. Bertoldi, *Adv. Mater.* **2016**, 28, 1631.
- [27] N. Fang, D. Xi, J. Xu, M. Ambati, W. Srituravanich, C. Sun, X. Zhang, *Nat. Mater.* **2006**, 5, 452.
- [28] N. Sui, X. Yan, T.-Y. Huang, J. Xu, F.-G. Yuan, Y. Jing, *Appl. Phys. Lett.* **2015**, 106, 171905.
- [29] H.-W. Dong, S.-D. Zhao, Y.-S. Wang, L. Cheng, C. Zhang, *J. Mech. Phys. Solids* **2020**, 137, 103889.
- [30] Z. Liu, X. Zhang, Y. Mao, Y. Y. Zhu, Z. Yang, C. T. Chan, P. Sheng, *Science* **2000**, 289, 1734.
- [31] X. An, C. Lai, H. Fan, C. Zhang, *Int. J. Solids Struct.* **2020**, 191–192, 293.
- [32] C. Pouya, J. T. B. Overvelde, M. Kolle, J. Aizenberg, K. Bertoldi, J. C. Weaver, P. Vukusic, *Adv. Opt. Mater.* **2016**, 4, 99.
- [33] M. Saba, M. Thiel, M. D. Turner, S. T. Hyde, M. Gu, K. Grosse-Brauckmann, D. N. Neshev, K. Mecke, G. E. Schröder-Turk, *Phys. Rev. Lett.* **2011**, 106, 103902.
- [34] K. Hur, Y. Francescato, V. Giannini, S. A. Maier, R. G. Hennig, U. Wiesner, *Angew. Chem. Int. Ed.* **2011**, 50, 11985.
- [35] Y. Jung, S. Torquato, *Phys. Rev. E* **2005**, 72, 056319.
- [36] H. Montazerian, E. Davoodi, M. Asadi-Eydivand, J. Kadkhodapour, M. Solati-Hashjin, *Mater. Des.* **2017**, 126, 98.
- [37] Z. A. Qureshi, S. A. B. Al Omari, E. Elnajjar, F. Mahmoud, O. Al-Ketan, R. A. Al-Rub, *Case Stud. Therm. Eng.* **2021**, 27, 101315.
- [38] O. Al-Ketan, R. K. A. Al-Rub, *Adv. Eng. Mater.* **2019**, 21, 1900524.
- [39] C. A. Aubin, B. Gorissen, E. Milana, P. R. Buskohl, N. Lazarus, G. A. Slipper, C. Keplinger, J. Bongard, F. Iida, J. A. Lewis, R. F. Shepherd, *Nature* **2022**, 602, 393.
- [40] A. H. Schoen, in *NASA Technical Note TN D-5541*, **1970**, pp. 1–100, <https://ntrs.nasa.gov/api/citations/19700020472/downloads/19700020472.pdf>.
- [41] M. R. J. Scherer, in *Double-Gyroid-Structured Functional Materials: Synthesis and Applications*, Springer Theses, Springer International Publishing, Cham **2013**.

- [42] H. G. von Schnering, R. Nesper, *Z. Phys. B Condens. Matter* **1991**, 83, 407.
- [43] D. Garoz, F. Gilabert, R. Sevenois, S. Spronk, W. Van Paepegem, *Composites Part B* **2019**, 168, 254.
- [44] W. Wu, J. Owino, A. Al-Ostaz, L. Cai, in *SIMULIA Community Conf.*, Providence **2014**, pp. 707–719.
- [45] D. Li, W. Liao, N. Dai, Y. M. Xie, *Materials* **2019**, 12, 2183.
- [46] S. C. Kapfer, S. T. Hyde, K. Mecke, C. H. Arns, G. E. Schröder-Turk, *Biomaterials* **2011**, 32, 6875.
- [47] O. Al-Ketan, R. Rezgui, R. Rowshan, H. Du, N. X. Fang, R. K. Abu Al-Rub, *Adv. Eng. Mater.* **2018**, 20, 1800029.
- [48] L. Gibson, M. Ashby, in *Cellular Solids: Structure and Properties*, Cambridge Solid State Science Series, Cambridge University Press, Cambridge, England **1997**.